ASPS Conference Proceedings 1: 1253-1264 (2022)

Proceedings of

12th Structural Engineering Convention-An International Event (SEC 2022)

Available at https://asps-journals.com/index.php/acp

Dynamic Performance Enhancement of One-way Reinforced Concrete Slabs by Fiber-reinforced Polymer Re-bars and Aluminum Foam under Air-blast Loading

S.M Anas [1, *], Mehtab Alam [2], Mohammad Umair [3]

[1] Department of Civil Engineering, Ph.D. Scholar, Jamia Millia Islamia, New Delhi, 110 025, India
[2] Department of Civil Engineering, Professor, Jamia Millia Islamia, New Delhi, 110 025, India
[3] Department of Civil Engineering, Assistant Professor, Jamia Millia Islamia, New Delhi, 110 025, India

Paper ID - 090419

Abstract

In the present study, finite element (FE) simulations are performed using the high fidelity physics-based finite element program, ABAQUS/CAE on the models of the one-way normal strength concrete slab, reinforced with the High Yield Strength Deformed (HYSD) steel re-bars, subjected to air-blast loading. The FE models are developed and subjected to different quantities of the TNT explosive charges at different scaled distances (between 0.75 and 3.0 m/kg$^{1/3}$) in free air. There exists a good correlation between available experimental values/observations and the results obtained analytically. Analyses have been extended replacing the conventional steel re-bars with the re-bars of the fiber-reinforced polymers namely; aramid, basalt, carbon, and glass, of equivalent strength on the tension side, impact side only, and both the sides of the slab. The replacement has been considered to improve the blast resistance of the slab. The damage in the slabs has been simulated using the available sophisticated material model to evaluate geometric parameters of cracks. FE simulation results for the considered combinations of the reinforcement have been compared to arrive at the best reinforcement combination in the slab. To further enhance the blast performance of this slab, single and double layers of the aluminum foam has also been considered on the impact face. Application of the aluminum foam is found to be effective in reducing the mid-span deflection, damage dissipation energy, and depth of transverse flexural cracks.

Keywords: Air-blast load, Concrete slab, Fiber reinforced polymer (FRP) re-bars, Aluminum foam, Explicit finite element analysis, Cracks, Damage, Damage dissipation energy

1. Introduction

Protection of military and civil structures from explosive-induced air-blast loads is receiving attention from structural designers due to the increased subversive blasts and accidental explosions in recent years [8, 11, 23]. The recent Beirut explosion (August 2020) witnesses this fact. Consequently, it is of paramount importance to assess the damage and improve the response of structures or structural elements subjected to explosive-induced blast loading.

Conventional steel re-bars are the most commonly used structural material in the construction of the reinforced concrete (RC) components [6]. Under certain environments, corrosion of the conventional steel re-bars can lead to deterioration or even failure of critical structural members [6]. Many attempts have been made in recent decades to address the corrosion problem, including the use of the fusion bonded epoxy coated re-bars (FBEC), corrosion-resistant steel deformed re-bars (CRSD), and the cement-polymer composite coated re-bars (CPCC) as alternatives to the conventional reinforcement (Singh N. D. D. and Ghosh R., 2001 [27]; Tang F. et al., 2012 [30]; Kamde K. D. and Pillai G. R., 2020 [17]). Recently, the use of the fiber-reinforced polymer (FRP) composites has been developed as a suitable approach to improve the load-carrying capacity of concrete members subjected to extreme loadings (Sim J. et al., 2005 [26]; Wu C. et al., 2009 [36]; Herwig A. and Motavalli M., 2012 [13]; Feng J. et al., 2017 [6]; Soltani H. et al., 2020 [28]). FRP is a composite material made of a resin matrix reinforced with fibers. The fibers widely used are aramid, basalt, carbon, and glass [6]. Another approach is to reduce the damage by protecting concrete structures with the external elements like steel plates or aluminum foams [4, 23]. The present investigation has two goals: (1) To investigate the blast response of the slabs by replacing the conventional reinforcement with the equivalent FRP reinforcement on the tension side, compression side only, and both the sides of the slab; and (2) To study the capabilities of the aluminum foam to act as a blast protective layer. Aluminum foams have been widely used in recent decades to reduce the damage and to dissipate energy as a cellular solid (Seitzberger M. et al., 2000 [24]; Gama A. B. et al., 2001 [7]; McCormack M. T. et al., 2001 [22]; Chen C. et al., 2001 [5]; Hanssen G. A. et al., 2002 [10]; Schenker A. et al., 2008 [23]). This study is of prime interest to the structural engineers and interested practitioners to analyze and design RC structures subjected to blast loading.

*Corresponding author. Tel: +918527764166; E-mail address: mohdanas43@gmail.com

Published online: December 19, 2022
doi:10.38208/acp.v1.649

Both experimental and analytical investigations have been conducted to study the effect of the charge mass, detonation distance, boundary condition, concrete strength, and reinforcement ratio on the blast response of reinforced concrete slabs (Xu K. and Lu Y., 2006 [37]; Zhou Q. X. et al., 2008 [39]; Wu C. et al., 2009 [36]; Silva F. P. and Lu B., 2009 [25]; Tai S. Y. et al., 2011 [29]; Wang W. et al., 2012 [33]; Wang W. et al., 2013 [34]; Zhao F. C. and Chen Y. J., 2013 [38]; Lin X. et al., 2014 [20]; Thiagarajan G. et al., 2015 [31]; Feng J. et al., 2017 [6]; Kumar V. et al., 2020 [18]). *Wu C. et al. (2009)* [36] tested a total of eight RC slabs to investigate the damage resistance under explosive-induced blast loading. The slabs were exposed to different quantities of the TNT charges detonated at different scaled distances (between 0.75 and 3.0 m/kg$^{1/3}$) in free air. Six out of eight slabs were constructed with the normal strength concrete, one slab constructed with the plain ultra-high-strength concrete, and one with the reinforced ultra-high-strength concrete. Two out of the six normal strength concrete slabs were retrofitted with the carbon fiber reinforced polymer (CFRP) sheets on impact face only. The dimension of all the slabs was 2000 mm in length, 1000 mm in width, and 100 mm in depth. The slabs were doubly reinforced with the 12 mm diameter High Yield Strength Deformed (HYSD) steel re-bars. The reinforcement was provided on both compression and tension faces at a spacing of 200 mm c/c in the minor bending plane (#12 mm @ 200 mm c/c) and 100 mm c/c in the major plane (#12 mm @ 100 mm c/c). The yield strength, ultimate tensile strength, and Young's modulus of the reinforcement were 600 MPa, 660 MPa, and 210 GPa, respectively. The thickness of the concrete cover was 10 mm. The 28-day average cylinder compressive strength of the normal strength concrete was 39.50 MPa, while that of the ultra-high-strength concrete was 150 MPa. Results revealed that the energy absorption capacity of the plain ultra-high-strength concrete slab was comparable to that of the normal reinforced concrete slab, however, the energy absorption capacity of the reinforced ultra-high-strength concrete slab was found superior to both the slabs. *Zhao F.C. and Chen Y. J. (2013)* [38] numerically investigated the effect of the explosive charge on the performance of 1000 mm x 1000 mm x 40 mm one-way singly reinforced concrete slabs subjected to near-field detonations using the Arbitrary Lagrangian-Eulerian (ALE) technique available in LS-DYNA software. Finite element simulation models were developed and subjected to different quantities of explosive charges at a fixed detonation distance of 0.40 m in free air. It was reported that the tension failure and spalling of concrete occurred on the bottom tension face near mid-span of the slabs. The analytical results revealed that the increase in the amount of the explosive charge increased the damage near the supports and formed more number of flexural cracks at the bottom tension face. *Thiagarajan G. et al. (2015)* [31] experimentally and numerically examined the performance of 1652 mm x 857 mm x 101.60 mm one-way concrete slabs with normal strength concrete (27.60 MPa) and high strength concrete (107 MPa) reinforced with the 9.50 mm diameter conventional, and HSLA-V steel re-bars subjected to peak reflected pressures by the shock tube (Blast Load Simulator) and using LS-DYNA software. Four types of slabs namely; NSC with conventional steel re-bars (NSC-NR), NSC with HSLA-V steel re-bars (NSC-VR), HSC with conventional steel re-bars (HSC-NR), and HSC with HSLA-V steel re-bars (HSC-VR) were studied. Transverse flexural cracks were observed on the tension face at the mid-span as well as at the supports of the target slabs. It was reported that the NSC-NR slab experienced the lowest peak reflected pressure and reflected impulse but highest mid-span deflection in comparison to HSC-NR. Comparing the deflection performance of HSC-NR and HSC-VR slabs, decreased in mid-span deflections found due to HSLA-V steel re-bars, calculated to be approximately 12.70%. HSLA-V steel re-bars lowered the mid-span deflections in the NSC slab by 45% (approx.). However, HSLA-V re-bars had performed better to reduce the number of transverse flexural cracks on the bottom tension face at the mid-span of the HSC slab. Results obtained from the numerical simulation were found to be in close agreement with those obtained from the experiment. *Feng J. et al. (2017)* [6] conducted a series of explosive tests to investigate the effect of reinforcement ratio on the blast response of 1100 mm x 1000 mm x 40 mm one-way concrete slabs reinforced with the conventional steel and basalt fiber reinforced polymer (BFRP) re-bars. A total of 12 slabs were tested. Three out of the twelve slabs were reinforced with the conventional steel re-bars of grade HPB 235. The average 28-day compressive strength of the concrete was 34.30 MPa. Cubical shaped TNT charges were detonated at different scaled distances (between 0.474 and 0.684 m/kg$^{1/3}$) in free air. Results indicated that the concrete slabs reinforced with the BFRP re-bars experienced lesser damage and maximum deflections than the slabs with steel re-bars. The general conclusion drawn was that the damage and maximum deflections reduced significantly with the increase of reinforcement ratio. *Kumar V. et al. (2020)* [18] conducted blast tests to investigate the damage resistance of 1000 mm x 1000 mm x 100 mm one-way RC slabs. A total of six slabs were tested and subjected to the cylindrical-shaped explosive charges ranging from 0.85 to 2.0 kg detonated at standoff distances of 0.10 m and 0.50 m in free air. The slabs were isotopically reinforced with the 10 mm diameter steel re-bars of grade Fe500 (IS 1786:2008). The results were compared and found to be in good agreement with the predictions of the Holmquist-Johnson-Cook (HJC) concrete material model available in the ABAQUS finite element program. They observed that the impact side (top face) of the RC slab failed due to the compressive failure and formation of the crater, while the rear side of the slab failed with the concrete spalling under higher blast pressures.

This paper investigates the blast response of one-way simply supported RC slabs using ABAQUS/CAE commercial software. A sophisticated material model has been utilized to evaluate geometric parameters of cracks. The goals of the present work are:

1. To develop finite element (FE) simulation models of the normal strength concrete slab, reinforced on both compression and tension sides with the steel re-bars, tested by Wu C. et al. (2009) [36] under different peak overpressures;
2. To validate analytical results with the available experimental values/observations;

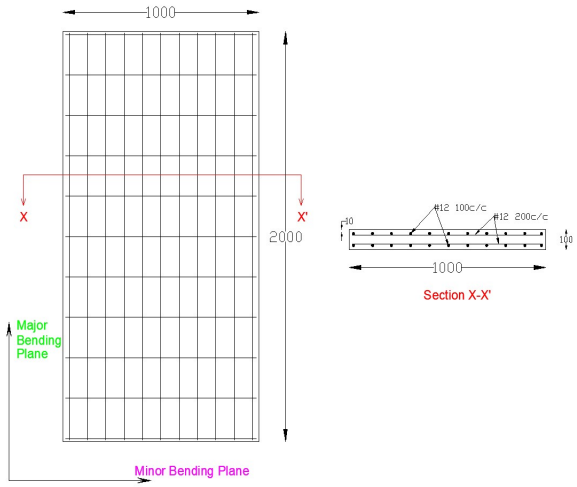

Fig. 1. Reinforcement detailing of the slab tested by Wu C. et al. (2009) [36]

3. To find out the most superior/inferior combinations of the reinforcement by replacing the conventional steel reinforcement with the FRP of equivalent strength on the tension side, impact side only, and both the sides of the slab;
4. To study the capabilities of the aluminum metal foam to mitigate the air-blast loads; and
5. To evaluate geometric parameters of cracks for the considered reinforcement combinations and scaled distances.

2. Numerical Modeling

A micro-modeling strategy has been adopted to develop finite element simulation models of the normal reinforced concrete slab tested by Wu C. et al. (2009) [36]. Fig.-1 shows the reinforcement detailing of the slab. The FE models are subjected to different quantities of the TNT charges at different scaled distances (between 0.75 and 3.0 m/kg$^{1/3}$) in free air. An explicit solver in ABAQUS/CAE finite element program has been employed to simulate the blast response of the slabs. The concrete is discretized with 8-node explicit solid elements (C3D8R) with hourglass control and reduced integration (ABAQUS User Assistance Manual, 2017). The re-bars are discretized with 3-node explicit second-order beam elements (B32). The re-bars are embedded into the concrete slab using embedded region constraint (see Fig.-2). The short edges of the slab are assumed constrained in all degrees of freedom. A mesh size of 10 mm has been adopted following the convergence test conducted at two different scaled distances (0.75 and 3.0 m/kg$^{1/3}$). The final mesh has 225,315 nodes and 200,440 elements (see Fig.-3).

2.1 FRP re-bar properties

The properties of the substituted polymer re-bars have been obtained from the study conducted by Brozda K. et al. (2017) [2] and are summarized in Table-1. It can be noted from Table-1 that the BFRP re-bars exhibit the highest mass density, while the CFRP re-bars have the largest tensile strength to density ratio. Table-2 lists the different combinations of the reinforcement considered in the present work. The equivalent cross-sectional area and diameter of the replaced FRP re-bars are summarized in Table-3.

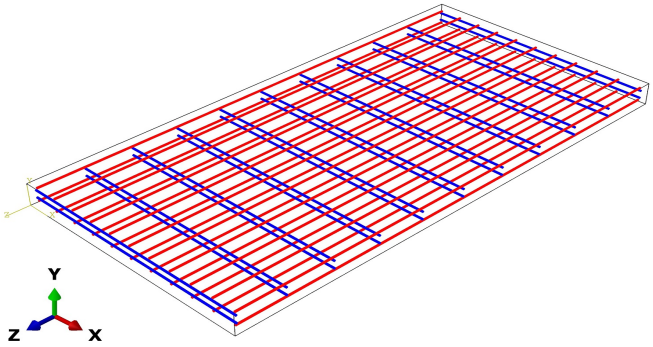

Fig. 2. Rendered view of the reinforcement

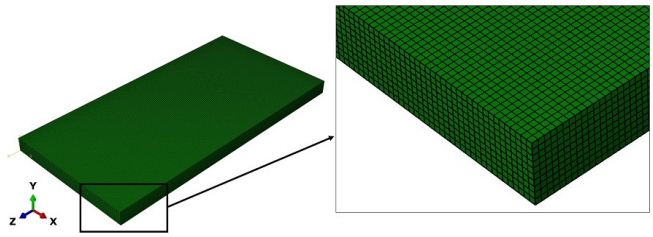

Fig. 3. FE mesh

Table-1. Properties of replaced polymer re-bars [2]

Type of FRP re-bar	Mechanical Properties				
	Density (kg/m^3)	Ultimate tensile strength (MPa)	Young's modulus (GPa)	Ultimate percentage elongation (%)	Tensile strength to density ratio
AFRP	1335	2541	85	3.16	1.90
BFRP	2135	1452	80	2.41	0.68
CFRP	1605	3102	150	1.71	1.93
GFRP	1955	1252	57	2.51	0.64

Table-2. Different combinations of reinforcement

Combination No.		Reinforcement	
		Tension Side (Remote face)	Compression Side (Impact face)
Q1	Q1-SS	HYSD steel re-bars	HYSD steel re-bars
Q2	Q2-AS	AFRP re-bars	HYSD steel re-bars
	Q2-BS	BFRP re-bars	HYSD steel re-bars
	Q2-CS	CFRP re-bars	HYSD steel re-bars
	Q2-GS	GFRP re-bars	HYSD steel re-bars
Q3	Q3-SA	HYSD steel re-bars	AFRP re-bars
	Q3-SB	HYSD steel re-bars	BFRP re-bars
	Q3-SC	HYSD steel re-bars	CFRP re-bars
	Q3-SG	HYSD steel re-bars	GFRP re-bars
Q4	Q4-AA	AFRP re-bars	AFRP re-bars
	Q4-BB	BFRP re-bars	BFRP re-bars
	Q4-CC	CFRP re-bars	CFRP re-bars
	Q4-GG	GFRP re-bars	GFRP re-bars

Table-3. Equivalent cross-sectional area and diameter of the replaced FRP re-bars

Properties	Reinforcing/Substitute material				
	Steel re-bars	AFRP re-bars	BFRP re-bars	CFRP re-bars	GFRP re-bars
Tensile strength (MPa)	660	2541	1452	3102	1252
Diameter of re-bar (mm)	12	^{e}6	^{e}8	^{e}6	^{e}10
Cross-sectional area of re-bar (mm^2)	113	^{f}28	^{f}50	^{f}28	^{f}79

* ^{e} Equivalent diameter to steel re-bar
* ^{f} Equivalent cross-sectional area of replaced FRP re-bar

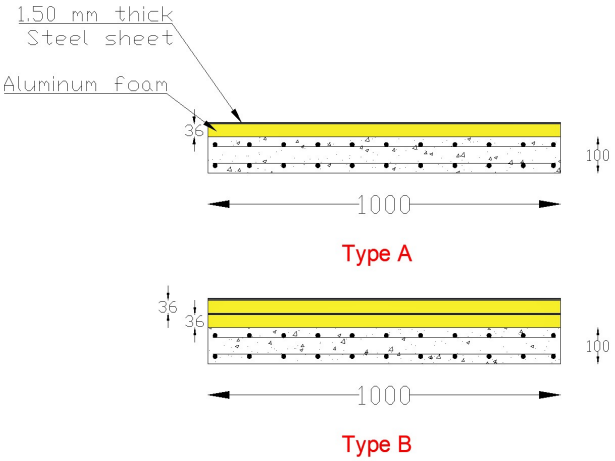

Fig. 4. Aluminum metal foam

2.2 Aluminum foam properties

In the present work, closed-cell aluminum foams are used and are applied on the top surface (blast face) of the slab in two ways: the first consisted of a single layer and the second consisted of two layers covered by a thin structural steel sheet (see Fig.-4). The effectiveness of aluminum foam as a blast protective layer has been examined only on the concrete slab having the best combination of the reinforcement. The input parameters including mass density, Young's modulus, simple shear test data, and uniaxial test data of the aluminum foam have been taken from the experimental study conducted by Schenker A. et al. (2008) [23]. The thickness of the metallic foam used is 36 mm. A surface-to-surface contact interaction, with "friction", "cohesive", and "hard" contact models, has been utilized to define the interaction between two surfaces namely; the master surface, and the slave surface [1]. Besides, the kinematic contact method with finite sliding has been adopted for mechanical contact formulation [1]. Aluminum foams are discretized with 8-node explicit solid elements (C3D8R) with reduced integration and hourglass control (ABAQUS User Assistance Guide, 2017). A mesh size of 9 mm has been adopted for the aluminum foam following the convergence test.

2.3 Air-blast loading, P(t)

Fig.-5 shows the typical explosive-induced air-blast pressure-time history produced from the ideal explosion, proposed by Wu C. and Hao H. (2005) [35]. In general, explosive-induced blast load is characterized by two phases namely; the positive phase, and the negative phase [3, 8, 15]. In the negative phase, the blast pressure falls below the ambient air pressure and a partial vacuum is formed. Current design guidelines for the blast protective structures usually recommend utilizing only the positive pressure phase of the blast load by assuming that the negative phase is normally much weaker and does not affect typical concrete structures [11]. Thus, the effect of the suction phase of the blast load on the blast response of the slabs has been neglected in the current study.

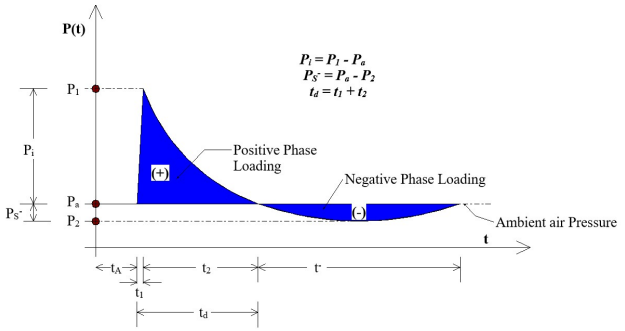

Fig. 5. Typical blast pressure profile [35]

Wu C. and Hao H. (2005) [35] experimentally investigated the effects of air-blast load and ground shock on concrete structures, and proposed several empirical equations to compute blast and ground shock wave parameters. They compared their results and found in good agreement with the predictions of TM 5-1300 (1990), *Structures to resist the effects of Accidental Explosions* [15]. Moreover, they simplified the positive phase of air-blast load into three parts: a constant ambient air pressure (P_a) followed by a sudden linear rise in air pressure to the peak value at the pressure front and then an exponential decay of the varying pressure, P(t). The following are the equations proposed by Wu C. and Hao H. (2005) [35] to define or model the time-dependent blast pressure, P(t):

$$t_A = 0.34\, R^{1.4}\, Q^{-0.2} / C_a \tag{1}$$

$$t_d = t_1 + t_2 \tag{2}$$

$$t_1 = 0.0019 \left(\frac{R}{Q^{\frac{1}{3}}}\right)^{1.30} \tag{3}$$

$$t_2 = 0.0005\, R^{0.72}\, Q^{0.16} \tag{4}$$

$$P(t) = \begin{Bmatrix} P_a; & (0 \le t < t_A) \\ P_a + P_i\left(\frac{t}{t_1}\right); & (t_A \le t \le t_1) \\ P_a + P_i\left(1 - \frac{t-t_1}{t_2}\right).exp\left(-\frac{\gamma(t-t_1)}{t_2}\right); & (t_1 \le t) \end{Bmatrix} \tag{5}$$

Here, Q = Weight of the charge (kg TNT); R = detonation distance (m); C_a = Speed of sound in air (≈340 m/sec); t_A = time of arrival of shock wave (sec); t_1 = rising time (sec); t_2 = decreasing time (sec); t_d = duration of positive phase of blast load (sec); P_a = ambient pressure (≈0.1 MPa); P_i = incident overpressure or peak overpressure (MPa); Z = scaled distance ($R/Q^{1/3}$, $m/kg^{1/3}$); and γ = decay of the curve. The decay constant (γ) can be calculated using the following equations [35]:

$$\gamma = \begin{Bmatrix} 3.02\, P_i^{0.38} + 6.85\, P_i^{0.79}.exp\left(-4.55\frac{t-t_1}{t_2}\right); & (t_1 \le t \le t_d) \\ 1.96\, P_i^{0.25} + 0.176\, P_i.exp\left(-0.73\, P_i^{-0.49}.\left(\frac{t-t_d}{t_2}\right)\right); & (t_d < t) \end{Bmatrix} \tag{6}$$

for P_i (MPa) $\leq$ 1.0,

$$\gamma = \begin{cases} 1.62\,P_i^{0.30} + 5.13\,P_i^{0.28}.exp\left(-1.05\,P_i^{0.37}.\left(\frac{t-t_1}{t_2}\right)\right); & (t_1 \leq t \leq t_d) \\ 0.74\,P_i^{0.17} + 2.71\,P_i^{0.28}.exp\left(-0.26\,P_i^{0.33}.\left(\frac{t-t_1}{t_2}\right)\right); & (t_d < t) \end{cases} \quad (7)$$

for 1.0 $<$ P_i (MPa) $\leq$ 100. The values of incident blast pressure (P_i) for different scaled distances have been taken from the experimental study conducted by Wu C. (2009) [36]. The estimated values of blast wave parameters are summarized in Table-4. Fig.-6 shows the estimated air-blast pressure profiles. The air-blast loading in ABAQUS/CAE program has been defined as pressure versus time application using an explicit solver. The blast pressure, P(t) has been applied to the top surface (impact face) of the target slab as shown in Fig.-7.

Table-4. Estimated values of air-blast wave parameters

Slab ID	Z (m/kg$^{1/3}$)	P_i (MPa)	t_A (ms)	t_l (ms)	t_d (ms)	Total duration, $t = t_A + t_d$ (ms)
RC 1	3.00	0.13	4.66	3.29	4.39	9.05
RC 2	1.50	0.54	3.08	0.16	1.70	4.78
RC 3	0.93	1.43	1.26	0.49	1.74	3.00
RC 4	0.75	1.72	1.17	0.16	1.23	2.40

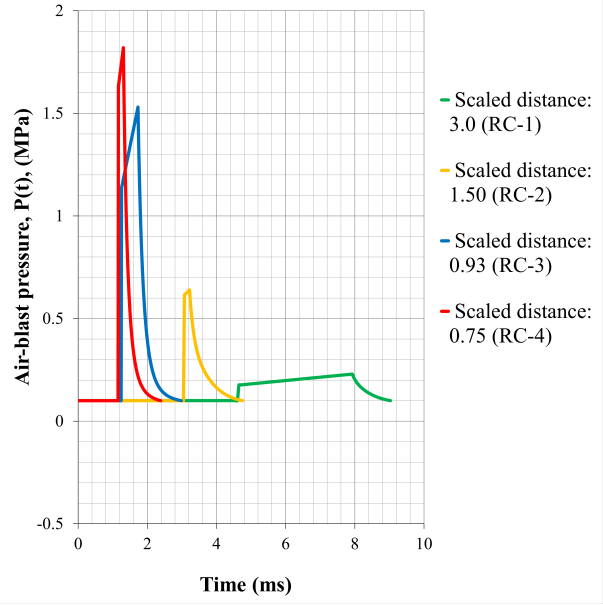

Fig. 6. Estimated blast pressure-time histories

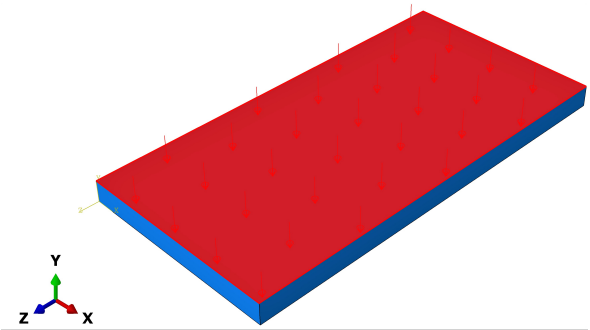

Fig. 7. Load application of blast pressure, P(t)

2.4 Material model

Numerous constitutive models for concrete have been developed to simulate the non-linear behavior of the concrete due to crushing in compression and cracking in tension (Ju W. J., 1989 [16]; Lee J. and Fenves L. G., 1998 [19]; Grassl P. and Jirasek M., 2006 [9]; Jason L. et al., 2006 [14]; Valentini B. and Hofstetter G., 2011 [32]). A very popular constitutive model is the concrete damaged plasticity model that combines plasticity and damage-mechanics theories [12]. In the present study, the concrete damaged plasticity (CDP) model available in the ABAQUS/CAE software has been employed to simulate the damage and to evaluate geometric parameters of cracks under the considered blast loading. The CDP model is a modification of the Drucker-Prager model proposed by Lubliner J. et al. (1989) [21] and Lee J. (1998) [19]. The evolution of the failure surface is controlled by two damage variables namely; compressive damage (d_c) and tensile damage (d_t), which are connected to failure mechanisms of the concrete under compression and tension loadings [1, 12]. It is assumed that the uniaxial stress-strain curves can be converted into stress versus inelastic-strain curves [1]. This conversion is performed automatically by the ABAQUS/CAE program from the user-provided stress versus plastic strain data. The uniaxial compressive and tensile responses of the material with respect to the CDP model under compression and tension loadings are given by:

$$\sigma_c = (1 - d_c)E_0(\varepsilon_c - \varepsilon_c^{pl,\ h}) \quad (8)$$

$$\sigma_t = (1 - d_t)E_0(\varepsilon_t - \varepsilon_t^{pl,\ h}) \quad (9)$$

Here, σ_c = nominal compressive stress; σ_t = nominal tensile stress; ε_c = Compressive strain ($\varepsilon_c^{pl,\ h} + \varepsilon_c^{el}$); ε_t = Tensile strain ($\varepsilon_t^{pl,\ h} + \varepsilon_t^{el}$); $\varepsilon_c^{pl,\ h}$ = plastic hardening compressive strain; $\varepsilon_t^{pl,\ h}$ = plastic hardening tensile strain; ε_c^{el} = elastic compressive strain; ε_t^{el} = elastic tensile strain; E_0 = initial elasticity modulus of material (undamaged); d_c and d_t are compression and tension damage variables ranging from zero (undamaged material) to one (total loss of strength).

Table-5. CDP material parameter table for concrete [12]

ψ	ε	f_{b0} / f_{c0}	K	μ
31°	0.10	1.16	0.67	0

Compressive Behavior		Compression Damage	
Yield Stress (MPa)	Inelastic Strain	Yield Stress (MPa)	Inelastic Strain
20.40	0	0	0
25.60	2.66667E-05	0	2.66667E-05
30.00	0.00008	0	0.00008
33.60	0.00016	0	0.00016
36.40	0.00026666	0	0.00026666
38.40	0.0004	0	0.0004
39.60	0.00056	0	0.00056
40.00	0.00074666	0	0.00074666
39.60	0.00096	0.01	0.00096
38.40	0.0012	0.04	0.0012
36.40	0.00146666	0.09	0.00146666
33.60	0.00176	0.16	0.00176
30.00	0.00208	0.25	0.00208
25.60	0.00242666	0.36	0.00242666
20.40	0.0028	0.49	0.0028
14.40	0.0032	0.64	0.0032
7.60	0.00362666	0.81	0.00362666
Tensile Behavior		Tension Damage	
Yield Stress (MPa)	Cracking Strain	Yield Stress (MPa)	Cracking Strain
4.00	0	0	0
0.04	0.00133333	0.99	0.00133333

The non-linear properties of concrete (39.50 MPa) taken from Hafezolghorani M. et al. (2017) [12] are listed in Table-5, where "ψ" is the dilation angle, "ε" is the flow potential eccentricity, "f_{b0} / f_{c0}" is the ratio of initial biaxial to initial uniaxial compressive yield stress, "K" is the ratio of the second stress invariant on the tensile meridian to that on the compressive meridian, and "μ" is the viscosity parameter.

3. Results and Discussion

3.1. Validation of FEA results

In order to validate the accuracy of the employed finite element program, maximum mid-span deflections and pattern of cracks generated from the finite element analysis are compared with the results of Wu C. et al. (2009) [36]. Comparisons of crack patterns obtained from the CDP model and Wu C. (2009) are shown in Fig.-8. Comparisons of maximum mid-span deflection obtained from FE analysis and Wu C. et al. (2009) [36] are listed in Table-6. The pattern of cracks and maximum mid-span deflections obtained from the FE analysis are in good agreement with available experimental results and the average absolute deviation is less than 3.0%. The reasonable difference indicates that the employed FE program can give a reliable prediction of maximum mid-span deflection and damage in the slabs subjected to explosive-induced blast loads.

Table-6. Comparison of maximum deflections

Slab No.	Q (kg)	Z (m/kg$^{1/3}$)	Maximum mid-span deflection in RC slab (mm)		Percentage difference (%)
			Experimental result (Wu C. et al., 2009)	FEA result	
RC 1	1.00	3.00	1.50	1.54	2.63
RC 2	8.00	1.54	10.50	10.44	0.57
RC 3	3.44	0.93	13.90	13.04	6.38
RC 4	8.00	0.75	38.90	38.57	0.85

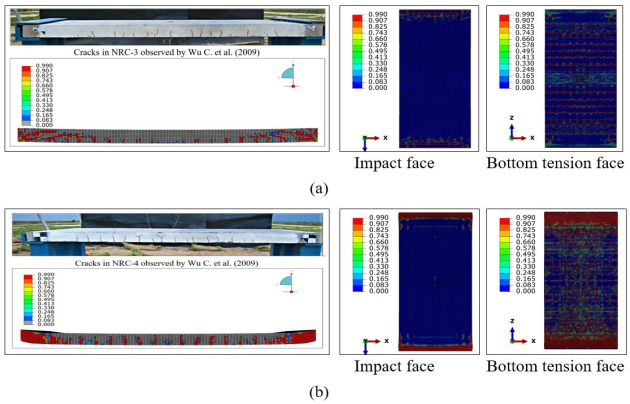

Fig. 8. Comparison of crack patterns for concrete slabs with steel re-bars on both faces: (a) RC 3 (t=3.00 ms), and (b) RC 4 (t=2.40 ms)

3.2. Replacement of the steel reinforcement by the equivalent FRP

Following the good correlation between available experimental values/observations and FE simulation results, further analysis has been conducted replacing the conventional reinforcement with the equivalent FRP on the tension side, impact side only, and both the sides of the slab. The substitution has been done to improve the blast performance of the slab. The maximum mid-span deflections in the slabs with different reinforcement combinations are summarized in Table-7to9. The deflection time histories for the different specimens and reinforcement combinations are shown in Fig.-9. In this study, the damage in the slabs has been observed in the form of concrete crushing near supports led by flexural-shear failure, development of transverse flexural and flexural-shear cracks, and damage dissipation energy. The computed values of damage dissipation energy in the slabs for different combinations of the reinforcement are summarized in Table-10to12. Higher the damage dissipation energy, more is the damage caused to the slab. The geometric parameters of cracks for the different specimens and reinforcement combinations are summarized in Table-13to17. The slabs with the substitution of the steel reinforcement by the equivalent FRP suffered lesser deflection and damage than the normal reinforced concrete slabs tested by Wu C. et al. (2009) [36], Table-7to12. Although, reduction of deflection and damage dissipation energy is maximum for the 100% replacement of the conventional reinforcement by the equivalent FRP reinforcement on both the sides of the slab (Q4), yet 100% substitution of the conventional reinforcement by the FRP reinforcement of equivalent strength on the tension side only (Q2) is found to be a more effective combination of the reinforcement under the applied blast loading. From deflection, damage, and cracking resistance points of view, the blast response of the concrete slab with the reinforcement combination Q2-CS is found to be the most superior to that with all other reinforcement combinations considered (Table-7,10&16). Moreover, the blast performance of the concrete slab with the reinforcement combination Q3-SG is found to be the poorest with regards to the cracking, deflection, and damage resistance (Table-8,11&16).

Table-7. Summary of maximum deflections for reinforcement combination Q2

Slab No.	Maximum mid-span deflection in the slabs (mm)				
	Q1-SS	Q2-AS	Q2-BS	Q2-CS	Q2-GS
RC 1	1.54	0.90 ([a]42%)	1.14 ([a]26%)	0.55 ([a]64%)	1.26 ([a]18%)
RC 2	10.44	7.31 ([a]30%)	8.84 ([a]15%)	6.66 ([a]36%)	9.00 ([a]14%)
RC 3	13.04	10.06 ([a]23%)	11.32 ([a]13%)	9.25 ([a]29%)	11.63 ([a]11%)
RC 4	38.57	32.70 ([a]15%)	35.36 ([a]8%)	29.98 ([a]22%)	36.21 ([a]6%)
Average percentage decrease in mid-span deflection		28%	16%	38%	12%

* [a] Percentage decrease with respect to Q1-SS (%)

Table-8. Summary of maximum deflections for reinforcement combination Q3

Slab No.	Maximum mid-span deflection in the slabs (mm)				
	Q1-SS	Q3-SA	Q3-SB	Q3-SC	Q3-SG
RC 1	1.54	1.13 ([a]27%)	1.30 ([a]16%)	0.98 ([a]36%)	1.38 ([a]10%)
RC 2	10.44	7.86 ([a]25%)	9.10 ([a]13%)	7.41 ([a]29%)	9.21 ([a]12%)
RC 3	13.04	10.74 ([a]18%)	11.82 ([a]9%)	10.07 ([a]23%)	12.11 ([a]7%)
RC 4	38.57	34.13 ([a]12%)	36.53 ([a]5%)	31.57 ([a]18%)	37.36 ([a]3%)
Average percentage decrease in mid-span deflection		21%	11%	27%	8%

* [a] Percentage decrease with respect to Q1-SS (%)

Table-9. Summary of maximum deflections for reinforcement combination Q4

Slab No.	Maximum mid-span deflection in the slabs (mm)				
	Q1-SS	Q4-AA	Q4-BB	Q4-CC	Q4-GG
RC 1	1.54	0.59 ([a]62%)	1.10 ([a]29%)	0.45 ([a]71%)	1.24 ([a]19%)
RC 2	10.44	6.99 ([a]33%)	8.96 ([a]14%)	5.96 ([a]43%)	9.11 ([a]13%)
RC 3	13.04	10.07 ([a]23%)	11.31 ([a]13%)	8.56 ([a]34%)	11.51 ([a]12%)
RC 4	38.57	33.23 ([a]14%)	36.41 ([a]6%)	28.71 ([a]26%)	36.91 ([a]4%)
Average percentage decrease in mid-span deflection		33%	16%	43%	12%

* [a] Percentage decrease with respect to Q1-SS (%)

Table-10. Summary of damage dissipation energy in the slabs with reinforcement combination Q2

Slab No.	Cumulative damage dissipation energy (J)				
	Q1-SS	Q2-AS	Q2-BS	Q2-CS	Q2-GS
RC 1	87.90	57.83 ([a]34%)	70.95 ([a]19%)	27.67 ([a]69%)	76.18 ([a]13%)
RC 2	1679.25	249.71 ([a]85%)	447.88 ([a]73%)	217.76 ([a]87%)	503.45 ([a]70%)
RC 3	7703.35	5754.18 ([a]25%)	6103.32 ([a]21%)	4272.65 ([a]45%)	6488.67 ([a]16%)
RC 4	64070.65	43175.83 ([a]33%)	52602.79 ([a]18%)	36690.70 ([a]43%)	56072.37 ([a]12%)
Average percentage decrease in damage dissipation energy		44%	33%	61%	28%

* [a] Percentage decrease with respect to Q1-SS (%)

Table-11. Summary of damage dissipation energy in the slabs with reinforcement combination Q3

Slab No.	Cumulative damage dissipation energy (J)				
	Q1-SS	Q3-SA	Q3-SB	Q3-SC	Q3-SG
RC 1	87.90	70.65 ([a]20%)	77.49 ([a]12%)	63.46 ([a]29%)	80.29 ([a]9%)
RC 2	1679.25	268.59 ([a]84%)	611.08 ([a]64%)	237.74 ([a]86%)	613.76 ([a]63%)
RC 3	7703.35	4538.14 ([a]41%)	5315.96 ([a]31%)	4249.96 ([a]45%)	5631.42 ([a]27%)
RC 4	64070.65	45852.24 ([a]28%)	52661.74 ([a]18%)	39724.79 ([a]38%)	53455.90 ([a]17%)
Average percentage decrease in damage dissipation energy		43%	31%	50%	29%

* [a] Percentage decrease with respect to Q1-SS (%)

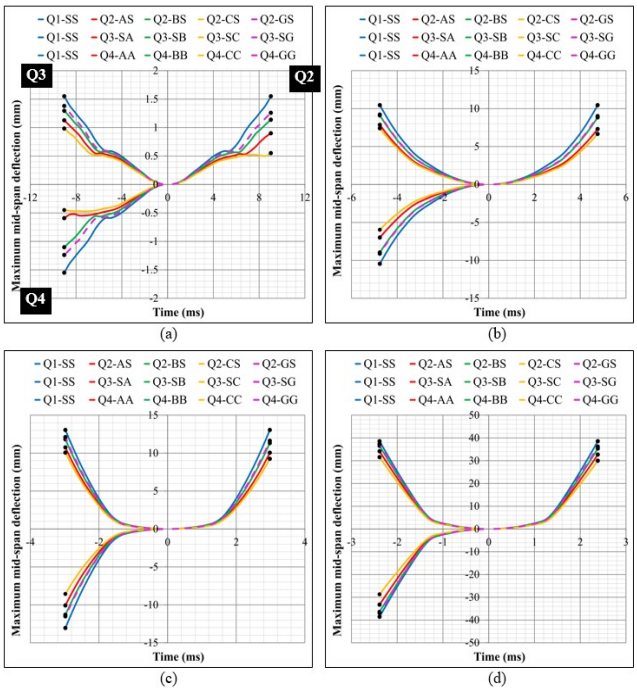

Fig. 9. Deflection – time histories of different specimens: (a) RC 1 (t=9.05 ms), (b) RC 2 (t=4.78 ms), (c) RC 3 (t=3.00 ms), and (d) RC 4 (t=2.40 ms)

FE simulation results show that the slabs only suffer flexural deformation. With the decrease of proximity factor (Z), the damage mode changes from the formation of flexural cracks on the rear surface (tension side) to the development of longitudinal, flexural-shear, and flexural cracks on both surfaces of the slab (Table-18). Also, crushing of concrete led by flexural-shear failure occurred near the supports of the slab RC 4 which is subjected to blast pressure of 1.72 MPa at a scaled distance of 0.75 m/kg$^{1/3}$ (see Fig.-10).

3.3. Effectiveness of aluminum foam to mitigate air-blast loads

In order to determine the effectiveness of aluminum foam as a blast protective layer, analysis has been conducted on the concrete slab with the reinforcement combination Q2-CS. Single and double composite layers of the aluminum foam and steel sheet are applied to the impact face (top surface) of the slab as shown in Fig.-4. Analytical results reveal that the unprotected slab experienced more deflection and damage than the slab protected with aluminum foam layers (Fig.-12to14).

A single protecting layer of aluminum foam and steel sheet reduced the mid-span deflection in the concrete slab with reinforcement combination Q2-CS by approximately 26% and crack depth by 21% (Table-19&21). Whereas, double aluminum foam layer decreased the mid-span deflection in the slab with reinforcement combination Q2-CS by approximately 40% and crack depth by 38%. This shows that aluminum foam improves the stiffness of the target slab by absorbing the shock. However, two layers of the aluminum foam along with steel sheet are found immensely effective in enhancing the damage resistance of the slab with reinforcement combination Q2-CS as compared to a single protecting layer of the foam and sheet.

Table-12. Summary of damage dissipation energy in the slabs with reinforcement combination Q4

Slab No.	Cumulative damage dissipation energy (J)				
	Q1-SS	Q4-AA	Q4-BB	Q4-CC	Q4-GG
RC 1	87.90	30.51 ([a]65%)	68.30 ([a]22%)	2.00 ([a]98%)	74.53 ([a]15%)
RC 2	1679.25	212.23 ([a]87%)	383.94 ([a]77%)	192.97 ([a]89%)	409.46 ([a]76%)
RC 3	7703.35	4803.08 ([a]38%)	5090.04 ([a]34%)	3236.83 ([a]58%)	5312.63 ([a]31%)
RC 4	64070.65	41348.29 ([a]35%)	44666.40 ([a]30%)	31849.88 ([a]50%)	51209.57 ([a]20%)
Average percentage decrease in damage dissipation energy		56%	41%	74%	35%

* [a] Percentage decrease with respect to Q1-SS (%)

Table-13. Average spacing of transverse cracks in slab RC 2 for different reinforcement combinations

Combination No.	Average spacing of transverse cracks (mm)			
	Impact face		Tension face	
	Q_{Span} (L/4)	M_{Span}	Q_{Span} (L/4)	M_{Span}
Q1-SS	f ([g]90)	-	-	67 ([m]15, [g]40)
Q2-AS	f ([g]80)	-	-	29 ([m]12, [g]33)
Q2-BS	f ([g]80)	-	-	27 ([m]15, [g]35)
Q2-CS	10, f ([m]2, [g]50)	-	-	28 ([m]16, [g]31)
Q2-GS	f ([g]90)	-	-	21 ([m]22, [g]36)
Q3-SA	f ([g]90)	-	-	51 ([m]16, [g]36)
Q3-SB	f ([g]90)	-	-	79 ([m]12, [g]38)
Q3-SC	f ([g]90)	-	-	30 ([m]20, [g]35)
Q3-SG	f ([g]90)	-	-	78 ([m]12, [g]39)
Q4-AA	f ([g]90)	-	-	25 ([m]16, [g]31)
Q4-BB	f ([g]90)	-	-	31 ([m]15, [g]34)
Q4-CC	f ([g]90)	-	-	47 ([m]11, [g]30)
Q4-GG	f ([g]90)	-	-	28 ([m]17, [g]34)

* Q_{Span} Quarter-span * M_{Span} Mid-span
* [m] Number of cracks developed * [g] Average depth of cracks (mm)
* [f] Flexural shear crack near supports

Table-14. Average spacing of longitudinal cracks in slab RC 3 for different reinforcement combinations

Combination No.	Average spacing of longitudinal cracks (mm)			
	Impact face		Tension face	
	W/4	W/2	W/4	W/2
Q1-SS	35 ([m]3, [g]30)	120 ([m]4, [g]20)	10 ([m]2, [g]20)	-
Q2-AS	-	-	-	-
Q2-BS	10 ([m]2, [g]10)	380 ([m]2, [g]10)	-	-
Q2-CS	-	-	-	-
Q2-GS	10 ([m]2, [g]15)	380 ([m]2, [g]10)	-	-
Q3-SA	-	-	-	-
Q3-SB	-	-	-	-
Q3-SC	-	-	-	-
Q3-SG	-	10 ([m]2, [g]30)	-	-
Q4-AA	-	10 ([m]2, [g]30)	-	-
Q4-BB	-	-	-	-
Q4-CC	-	-	-	-
Q4-GG	-	-	-	-

* [m] Number of cracks developed * [g] Average depth of cracks (mm)

Table-15. Average spacing of transverse cracks in slab RC 3 for different reinforcement combinations

Combination No.	Average spacing of transverse cracks (mm)			
	Impact face		Tension face	
	Q_{Span} (L/4)	M_{Span}	Q_{Span} (L/4)	M_{Span}
Q1-SS	23, f ([m]4, [g]50)	-	54 ([m]7, [g]58)	63 ([m]14, [g]49)
Q2-AS	40, f ([m]2, [g]50)	-	85 ([m]3, [g]50)	56 ([m]12, [g]29)
Q2-BS	f ([g]80)	-	43 ([m]5, [g]53)	44 ([m]13, [g]35)
Q2-CS	f ([g]80)	-	34 ([m]4, [g]43)	43 ([m]13, [g]27)
Q2-GS	30, f ([m]2, [g]55)	-	38 ([m]5, [g]54)	51 ([m]15, [g]36)
Q3-SA	f ([g]85)	-	23 ([m]7, [g]45)	78 ([m]10, [g]32)
Q3-SB	f ([g]85)	-	48 ([m]6, [g]46)	96 ([m]11, [g]37)
Q3-SC	f ([g]85)	-	58 ([m]5, [g]42)	101 ([m]10, [g]32)
Q3-SG	f ([g]85)	-	25 ([m]8, [g]50)	85 ([m]10, [g]39)
Q4-AA	f ([g]78)	-	45 ([m]5, [g]50)	49 ([m]12, [g]25)
Q4-BB	f ([g]78)	-	47 ([m]4, [g]50)	48 ([m]10, [g]31)
Q4-CC	f ([g]78)	-	30 ([m]5, [g]50)	28 ([m]14, [g]26)
Q4-GG	f ([g]78)	-	27 ([m]7, [g]50)	45 ([m]15, [g]34)

* Q_{Span} Quarter-span * M_{Span} Mid-span
* [m] Number of cracks developed * [g] Average depth of cracks (mm)
* [f] Flexural shear crack near supports

Table-16. Average spacing of transverse cracks in slab RC 4 for different reinforcement combinations

Combination No.	Average spacing of transverse cracks (mm)			
	Impact face		Tension face	
	Q_{Span} (L/4)	M_{Span}	Q_{Span} (L/4)	M_{Span}
Q1-SS	h ([g]98)	-	35 ([m]10, [g]80)	87 ([m]16, [g]85)
Q2-AS	h ([g]98)	200 ([m]2, [g]98)	24 ([m]12, [g]73)	69 ([m]14, [g]63)
Q2-BS	h ([g]98)	85 ([m]5, [g]98)	30 ([m]11, [g]70)	50 ([m]21, [g]65)
Q2-CS	h ([g]98)	10 ([m]2, [g]98)	31 ([m]8, [g]72)	52 ([m]13, [g]60)
Q2-GS	h ([g]98)	104 ([m]5, [g]98)	33 ([m]9, [g]73)	60 ([m]17, [g]69)
Q3-SA	h ([g]98)	-	25 ([m]10, [g]51)	65 ([m]12, [g]74)
Q3-SB	h ([g]98)	-	29 ([m]11, [g]53)	81 ([m]13, [g]74)
Q3-SC	h ([g]98)	-	30 ([m]8, [g]55)	86 ([m]11, [g]74)
Q3-SG	h ([g]98)	-	32 ([m]9, [g]57)	68 ([m]12, [g]75)
Q4-AA	h ([g]98)	-	19 ([m]11, [g]55)	44 ([m]15, [g]61)
Q4-BB	h ([g]98)	-	21 ([m]9, [g]62)	53 ([m]16, [g]64)
Q4-CC	h ([g]98)	10 ([m]2, [g]98)	27 ([m]8, [g]63)	69 ([m]14, [g]58)
Q4-GG	h ([g]98)	10 ([m]2, [g]98)	19 ([m]11, [g]62)	66 ([m]16, [g]65)

* Q_{Span} Quarter-span * M_{Span} Mid-span
* [m] Number of cracks developed * [g] Average depth of cracks (mm)
* [h] Crushing of concrete led by flexural-shear failure at supports

Table-17. Average spacing of longitudinal cracks in slab RC 4 for different reinforcement combinations

Combination No.	Average spacing of longitudinal cracks (mm)			
	Impact face		Tension face	
	W/4	W/2	W/4	W/2
Q1-SS	85 (^{m}3, ^{g}100)	-	80 (^{m}7, ^{g}85)	85 (^{m}8, ^{g}73)
Q2-AS	20 (^{m}2, ^{g}100)	165 (^{m}3, ^{g}100)	43 (^{m}4, ^{g}90)	78 (^{m}5, ^{g}80)
Q2-BS	20 (^{m}2, ^{g}100)	70 (^{m}3, ^{g}100)	105 (^{m}5, ^{g}83)	75 (^{m}5, ^{g}87)
Q2-CS	100 (^{m}2, ^{g}100)	50 (^{m}2, ^{g}100)	40 (^{m}2, ^{g}80)	185 (^{m}3, ^{g}83)
Q2-GS	85 (^{m}3, ^{g}100)	175 (^{m}3, ^{g}100)	40 (^{m}3, ^{g}70)	115 (^{m}5, ^{g}90)
Q3-SA	64 (^{m}5, ^{g}93)	85 (^{m}3, ^{g}100)	53 (^{m}2, ^{g}80)	88 (^{m}5, ^{g}58)
Q3-SB	38 (^{m}6, ^{g}100)	85 (^{m}4, ^{g}100)	63 (^{m}4, ^{g}85)	85 (^{m}6, ^{g}56)
Q3-SC	15 (^{m}5, ^{g}100)	95 (^{m}3, ^{g}100)	85 (^{m}3, ^{g}30)	87 (^{m}4, ^{g}70)
Q3-SG	53 (^{m}5, ^{g}100)	180 (^{m}2, ^{g}100)	83 (^{m}4, ^{g}60)	88 (^{m}7, ^{g}76)
Q4-AA	15 (^{m}6, ^{g}100)	205 (^{m}3, ^{g}100)	-	103 (^{m}5, ^{g}56)
Q4-BB	43 (^{m}7, ^{g}100)	70 (^{m}5, ^{g}100)	90 (^{m}3, ^{g}92)	107 (^{m}5, ^{g}75)
Q4-CC	10 (^{m}2, ^{g}95)	260 (^{m}2, ^{g}100)	-	170 (^{m}3, ^{g}73)
Q4-GG	40 (^{m}6, ^{g}100)	43 (^{m}4, ^{g}100)	45 (^{m}2, ^{g}90)	83 (^{m}5, ^{g}68)

* Q_{Span} Quarter-span * M_{Span} Mid-span
* ^{m} Number of cracks developed * ^{g} Average depth of cracks (mm)
* ^{h} Crushing of concrete led by flexural-shear failure at supports

Table-18. Observed damage levels

Slab No.	Z (m/kg$^{1/3}$)	Damage level	Remarks
RC 1	3.00	Low damage	• No perceptible cracks
RC 2	1.54	Moderate damage	• Transverse flexural cracks on tension side only; • Detachment of concrete cover on impact face • No crushing of concrete
RC 3	0.93	High damage	• Formation of flexural-shear and flexural cracks on tension side; • Few longitudinal cracks on impact face; • No concrete crushing
RC 4	0.75	Severe damage	• Crushing of concrete near supports led by flexural-shear failure; • Significant number of cracks in longitudinal and transverse directions on both sides of the slab

Table-19. Summary of maximum deflection in the slab without and with aluminum foam

Slab No.	Maximum mid-span deflection in the slabs (mm)			
	Q1-SS	Q2-CS	Q2-CS + Aluminum foam (Type A)	Q2-CS + Aluminum foam (Type B)
RC 1	1.54	0.55	0.37 (^{a}76% ; ^{b}33%)	0.30 (^{a}81% ; ^{b}45%)
RC 2	10.44	6.66	4.09 (^{a}61% ; ^{b}39%)	2.84 (^{a}73% ; ^{b}57%)
RC 3	13.04	9.25	7.18 (^{a}45% ; ^{b}22%)	6.05 (^{a}54% ; ^{b}35%)
RC 4	38.57	29.98	26.99 (^{a}30%; ^{b}10%)	23.71 (^{a}39%; ^{b}21%)
Average percentage decrease in mid-span deflection			(^{a}53% ; ^{b}26%)	(^{a}62% ; ^{b}40%)

* ^{a} Percentage decrease with respect to Q1-SS (%)
* ^{b} Percentage decrease with respect to Q2-CS (%)

Table-20. Summary of damage dissipation energy in the slab without and with aluminum foam

Slab No.	Cumulative damage dissipation energy in the slab (J)			
	Q1-SS	Q2-CS	Q2-CS + Aluminum foam (Type A)	Q2-CS + Aluminum foam (Type B)
RC 1	87.90	27.67	17.58 (^{a}80% ; ^{b}36%)	8.79 (^{a}90% ; ^{b}68%)
RC 2	1679.25	217.76	167.92 (^{a}90% ; ^{b}23%)	100.75 (^{a}94% ; ^{b}54%)
RC 3	7703.35	4272.65	3774.64 (^{a}51% ; ^{b}12%)	3389.47 (^{a}56% ; ^{b}21%)
RC 4	64070.65	36690.70	33957.44 (^{a}47%; ^{b}7%)	30753.90 (^{a}52%; ^{b}16%)
Average percentage decrease in damage dissipation energy			(^{a}67% ; ^{b}20%)	(^{a}73% ; ^{b}40%)

* ^{a} Percentage decrease with respect to Q1-SS (%)
* ^{b} Percentage decrease with respect to Q2-CS (%)

Table-21. Average spacing of transverse flexural cracks in the slab without and with aluminum foam

Slab No.	Average spacing of transverse cracks at mid-span of the slab (mm)			
	Q1-SS	Q2-CS	Q2-CS + Aluminum foam (Type A)	Q2-CS + Aluminum foam (Type B)
RC 1	-	-	-	-
RC 2	67 (^{m}15, ^{g}40)	28 (^{m}16, ^{g}31)	74 (^{m}8, ^{g}25)	20 (^{m}4, ^{g}20)
RC 3	63 (^{m}14, ^{g}49)	43 (^{m}13, ^{g}27)	10 (^{m}2, ^{g}20)	10 (^{m}2, ^{g}17)
RC 4	87 (^{m}16, ^{g}85)	52 (^{m}13, ^{g}60)	58 (^{m}7, ^{g}50)	200 (^{m}4, ^{g}35)
Average percentage decrease in crack depth			(^{a}46% ; ^{b}21%)	(^{a}58% ; ^{b}38%)

* ^{m} Number of cracks developed * ^{g} Average depth of cracks (mm)
* ^{a} Percentage decrease with respect to Q1-SS (%)
* ^{b} Percentage decrease with respect to Q2-CS (%)

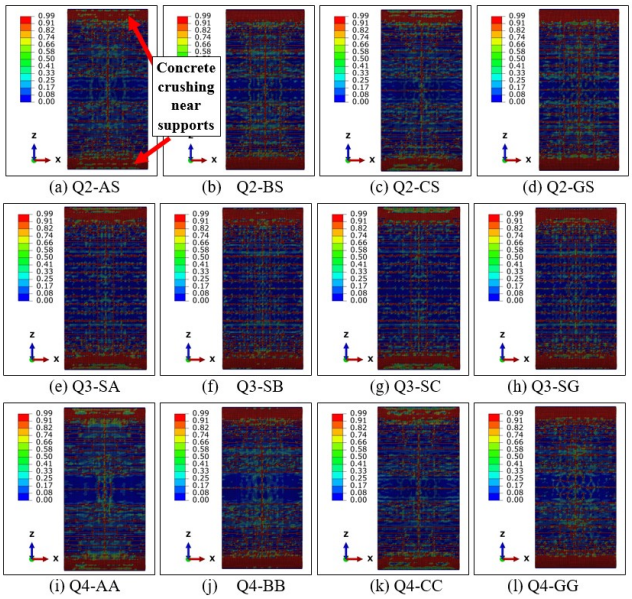

Fig. 10. Pattern of cracks on the bottom tension side of slab RC 4 for different reinforcement combinations (red color: "damaged material"; blue color: "undamaged material")

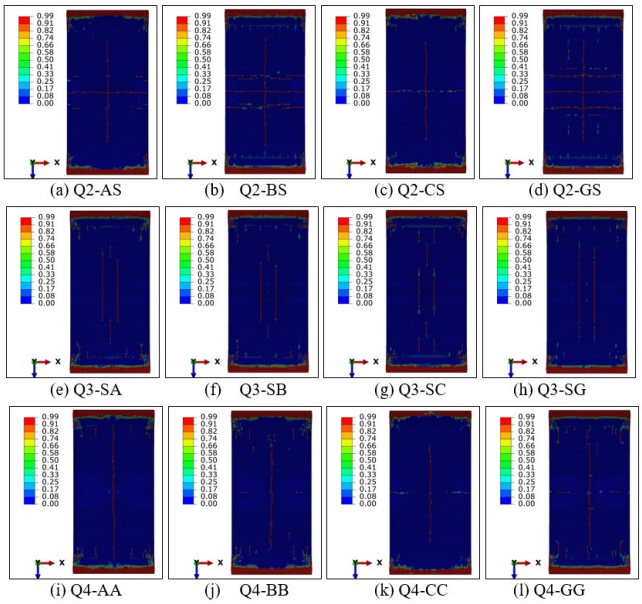

Fig. 11. Pattern of cracks on the impact face of slab RC 4 for different reinforcement combinations (red color: "damaged material"; blue color: "undamaged material")

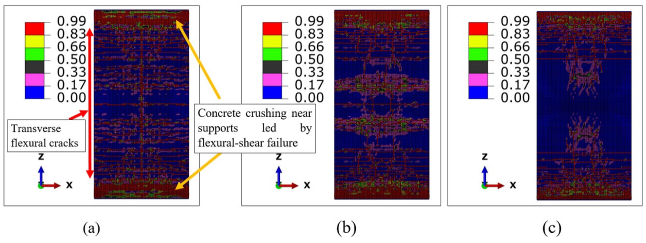

Fig. 12. Pattern of cracks on bottom tension side of slab RC 4 for different combinations: (a) Q2-CS, (b) Q2-CS + Type A, and (c) Q2-CS + Type B

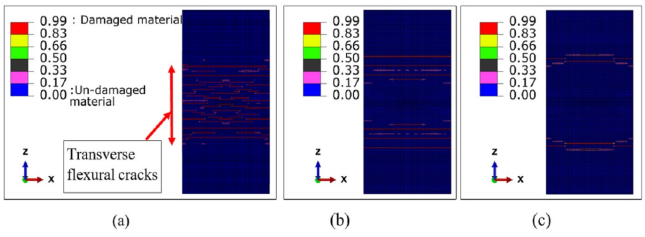

Fig. 13. Pattern of cracks on bottom tension side of slab RC 2 for different combinations: (a) Q2-CS, (b) Q2-CS + Type A, and (c) Q2-CS + Type B

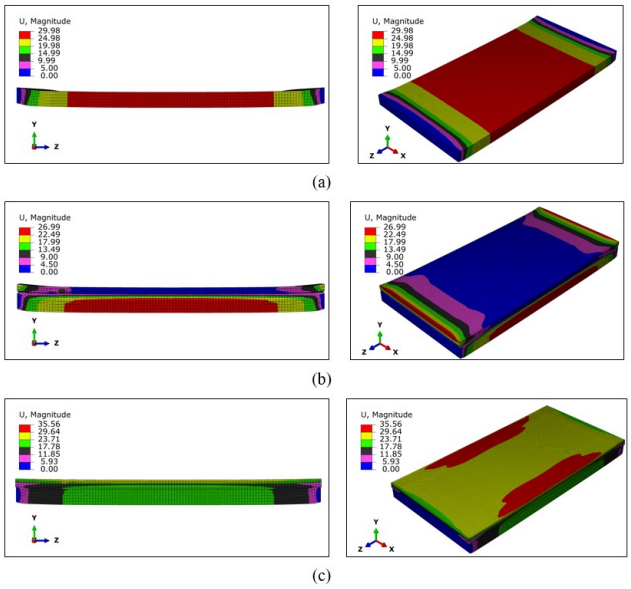

Fig. 14. Distribution of resultant displacement (mm) in slab RC 4 for different combinations: (a) Q2-CS, (b) Q2-CS + Type A, and (c) Q2-CS + Type B

4. Conclusions

Based on the finite element simulations results, the following conclusions are obtained:

1. Although, reduction of deflection and damage dissipation energy is maximum for the 100% conventional reinforcement replacement by the equivalent FRP on both the sides of the slab (Q4), yet 100% substitution by the FRP of equivalent strength on the tension side only (Q2) is found to be a more effective combination of the reinforcement under the applied blast loading.
2. For the considered combinations of the reinforcement, the concrete slab with the carbon-fiber-reinforced polymer re-bars on the tension side and the steel re-bars on the compression side (Q2-CS) gives the superior performance, while the slab with the glass fiber polymer re-bars on the compression side and the steel re-bars on the tension side (Q3-SG) gives the poorest performance under the applied blast pressures.
3. The concrete slab reinforced with the steel re-bars on the compression side with a single protecting layer of aluminum foam and sheet (Type A) and with the carbon-fiber-reinforced polymer re-bars on the tension side (Q2-CS) reduced the mid-span deflection by approximately 53% and damage dissipation energy by 67%, while the slab with the steel re-bars on the impact side with double layer of aluminum foam and steel sheet (Type B) and with the carbon fiber polymer re-bars on the tension side decreased the mid-span deflection by approximately 62% and damage dissipation energy by 73% in comparison to the concrete slab with the conventional reinforcement on both sides (Q1-SS). The double composite layer of aluminum foam and steel sheet is found to be more

effective in reducing the mid-span deflection, damage, and crack depth and hence can be adopted to mitigate the air-blast loads generated by explosions.

4. Application of the carbon-fiber-reinforced polymer re-bars on the tension side of the slab with the steel re-bars on the compression side (Q2-CS) is found to be giving the best performance under the considered blast loading without escalating the cost of the slab (Appendix A).

Acknowledgements

The authors gratefully acknowledge the computational facilities provided by the Head of the Civil Engineering Department, Faculty of Engineering and Technology, Jamia Millia Islamia, New Delhi-110025, India, for carrying out the present finite element simulations. Special thanks are due to Professor T K Datta from the Department of Civil Engineering at the Indian Institute of Technology Delhi, New Delhi-110016, India, for his assistance in blast dynamics.

Disclosures

Free Access to this article is sponsored by SARL ALPHA CRISTO INDUSTRIAL.

References

1. ABAQUS/CAE FEA program 2017. Concrete damaged plasticity model, explicit solver, three dimensional solid element library. ABAQUS DS-SIMULIA User Assistance Manual, 2017.
2. Brozda K, Selejdak J, and Kotes P. Analysis of properties of the FRP rebar to concrete structures. Applied Engineering Letters, 2017; 2(1): 6-10.
3. Bureau of Indian Standards. Criteria for blast resistant design of structures for explosions above ground. IS 4991(1968).
4. Castedo R, Segarra P, Alanon A, Lopez M L, Santos P A, Sanchidrian A J. Air blast resistance of full-scale slabs with different compositions: Numerical modeling and field validation. International Journal of Impact Engineering, 2015; 86: 145-156.
5. Chen C, Harte M A, and Fleck A N. The plastic collapse of sandwich beams with a metallic foam core. International Journal of Mechanical Sciences, 2001; 43: 1483-1506.
6. Feng J, Zhou Y, Wang P, Wang B, Zhou J, Chen H, Fan H, and Jin F. Experimental research on blast-resistance of one-way concrete slabs reinforced by BFRP bars under close-in explosion. Engineering Structures, 2017; 150: 550-561.
7. Gama A B, Bogetti A T, Fink K B, Yu J C, Claar D T, Eifert H H, Gillespie W J. Aluminum foam integral armor: a new dimension in armor design. Composite Structures, 2001; 52: 381-395.
8. Goel D M and Matsagar A V. Blast-resistant design of structures. Practice Periodical on Structural Design and Construction, 2014, ASCE, 19(2): 04014007-1-9.
9. Grassl P and Jirasek M. Damage-plastic model for concrete failure. International Journal of Solids and Structures, 2006; 43(22-23): 7166-7196.
10. Hanssen G A, Enstock L, and Langseth M. Close-range blast loading of aluminum foam panels. International Journal of Impact Engineering, 2002; 27: 593-618.
11. Hao H. Hao Y, Li J, and Chen W. Review of the current practices in blast-resistant analysis and design of concrete structures. Advances in Structural Engineering, 2016; 19(8): 1193-1223.
12. Hafezolghorani M, Hejazi F, Vaghei R, Jaafar B S M, and Karimzade K. Simplified damage plasticity model for concrete. Structural Engineering International, 2017; 27(1): 68-78.
13. Herwig A and Motavalli M. Axial behavior of square reinforced concrete columns strengthened with lightweight concrete elements and unbonded GFRP wrapping. Journal of Composites for Construction, 2012, ASCE, 16(6): 747-752.
14. Jason L, Huerta A, Cabot P G, Ghavamian S. An elastic plastic damage formulation for concrete: Application to elementary tests and comparison with an isotropic damage model. Computer Methods in Applied Mechanics and Engineering, 2006; 195(52): 7077-7092.
15. Joint Department of the Army, the Navy, and the Air Force. Structures to resist the effects of accidental explosions. Technical Manual, TM 5-1300(1990).
16. Ju W J. On energy-based coupled elastoplastic damage theories: Constitutive modeling and computational aspects. International Journal of Solids and Structures, 1989; 25(7): 803-833.
17. Kamde K D and Pillai G R. Effect of surface preparation on corrosion of steel rebars coated with cement-polymer-composites (CPC) and embedded in concrete. Construction and Building Materials, 2020; 237: 1-12.
18. Kumar V, Kartik V K, and Iqbal A M. Experimental and numerical investigation of reinforced concrete slabs under blast loading. Engineering Structures, 2020; 206: 110-125.
19. Lee J and Fenves L G. Plastic-damage model for cyclic loading of concrete structures. Journal of Engineering Mechanics, 1998, ASCE; 124(8).
20. Lin X, Zhang X Y, and Hazell J P. Modelling the response of reinforced concrete panels under blast loading. Materials & Design (1980-2015), 2014; 56: 620-628.
21. Lubliner J, Oliver J, Oller S, and Onate E. A plastic-damage model for concrete. International Journal of Solids and Structures, 1989; 25(3): 299-326.
22. McCormack M T, Miller R, Kesler O, and Gibson J L. Failure of sandwich beams with metallic foam cores. International Journal of Solids and Structures, 2001; 38: 4901-4920.
23. Schenker A, Anteby I, Gal E, Kivity Y, Nizri E, Sadot O, Michaelis R, Levintant O, Ben-Dor G. Full-scale field tests of concrete slabs subjected to blast loads. International Journal of Impact Engineering, Elsevier, 2008; 35: 184-198.
24. Seitzberger M, Rammerstorfer G F, Gradinger R, Degischer P H, Blaimschein M, and Walch C. Experimental studies on the quasi-static axial crushing of steel columns filled with aluminum foam. International Journal of Solids and Structures, 2000; 37: 4125-4147.
25. Silva F P and Lu B. Blast resistance capacity of reinforced concrete slabs. Journal of Structural Engineering, 2009, ASCE, 135(6).

26. Sim J, Park C, and Moon Y D. Characteristics of basalt fiber as a strengthening material for concrete structures. Composites: Part B, 2005; 36: 504-512.

27. Singh N D D and Ghosh R. Corrosion resistance performance of fusion bonded epoxy coated rebars. NSCP Conference, 2001; 113-121.

28. Soltani H, Khaloo A, and Sadraie H. Dynamic performance enhancement of RC slabs by steel fibers vs. externally bonded GFRP sheets under impact loading. Engineering Structures, 2020; 213: 1-21.

29. Tai S Y, Chu L T, Hu T H, Wu Y J. Dynamic response of a reinforced concrete slab subjected to air blast load. Theoretical and Applied Fracture Mechanics, 2011; 56(3): 140-147.

30. Tang F, Chen G, Brow K R, Volz S J, Koenigstein L M. Corrosion resistance and mechanism of steel rebar coated with three types of enamel. Corrosion Science, 2012; 59: 157-168.

31. Thiagarajan G, Kadambi V A, Robert S, and Johnson F C. Experimental and finite element analysis of doubly reinforced concrete slabs subjected to blast loads. International Journal of Impact Engineering, 2015; 75: 162-173.

32. Valentini B and Hofstetter G. Review and enhancement of 3D concrete models for large-scale numerical simulations of concrete structures. International Journal for Numerical and Analytical Methods in Geomechanics, 2011, Wiley; 37(3): 221-246.

33. Wang W, Zhang D, Lu F, Wang C S, and Tang F. Experimental study on scaling the explosion resistance of a one-way square reinforced concrete slab under a close-in blast loading. International Journal of Impact Engineering, 2012; 49: 158-164.

34. Wang W, Zhang D, Lu F, Wang C S, and Tang F. Experimental study and numerical simulation of the damage mode of a square reinforced concrete slab under close-in explosion. Engineering Failure Analysis, 2013; 27: 41-51.

35. Wu C and Hao H. Modeling of simultaneous ground shock and airblast pressure on nearby structures from surface explosions. International Journal of Impact Engineering, 2005; 31(6): 699-717.

36. Wu C, Oehlers J D, Rebentrost M, Leach J, and Whittaker S A. Blast testing of ultra-high performance fibre and FRP-retrofitted concrete slabs. Engineering Structures, 2009; 31: 2060-2069.

37. Xu K and Lu Y. Numerical simulation study of spallation in reinforced concrete plates subjected to blast loading. Computers & Structures, 2006; 84(5-6): 431-438.

38. Zhao F C and Chen Y J. Damage mechanism and mode of square reinforced concrete slab subjected to blast loading. Theoretical and Applied Fracture Mechanics, 2013; 63-64: 54-62.

39. Zhou Q X, Kuznetsov A V, Hao H, and Waschl J. Numerical prediction of concrete slab response to blast loading. International Journal of Impact Engineering, 2008; 35(10): 1186-1200.

Appendix A: Cost Estimation of Re-bars in the Concrete Slab

Length of the slab: 2 m
Width of the slab: 1 m

Tension Side:
No. of main bars: 11
No. of secondary bars: 11

Compression Side:
No. of main bars: 11
No. of secondary bars: 11

Diameter of steel re-bars: 12 mm
Cross-sectional area of steel re-bar: 113 mm^2

Equivalent diameter of CFRP re-bars: 6 mm (Table-3)
Equivalent cross-section area of CFRP re-bar: 28 mm^2

Rate (for 12 mm diameter steel re-bars): 59.13 INR / kg (i6 Fe-600 TMT Grade, "https://www.materialtree.com/bengaluru/i6-fe-600-tmt-grade")

Rate (for 6 mm diameter CFRP re-bars): 0.90 USD / m (Antop Global Technology Co., Ltd., China, "https://www.antopgfrp.com/fibre-polymer-rebar/carbon-fibre-polymer-rebar/carbon-fiber-rebar.html")

- *For reinforcement combination Q1-SS*:

Compression side: Fe-600 steel re-bars
Tension side: Fe-600 steel re-bars

Main bars: #12 @ 100 mm c/c
Secondary bars: #12 @ 200 mm c/c

For 12 mm diameter steel re-bars: 0.890 kg/m

Cost of main re-bars: 0.890 x 59.13 x 2 = 105.25 INR
Cost of secondary re-bars: 0.890 x 59.13 x 1 = 52.63 INR

Total cost of re-bars: 105.22 x 22 + 52.63 x 22 = 3472.70 INR

- *For reinforcement combination Q2-CS*:

Compression side: Fe-600 steel re-bars
Tension side: CFRP re-bars

Tension side:
Main bars: #6 @ 100 mm c/c
Secondary bars: #6 @ 200 mm c/c
Cost of main re-bars: 0.90 x 2 = 1.80 USD (132.92 INR)
Cost of secondary re-bars: 0.90 x 1 = 0.90 USD (66.46 INR)

Compression side:
Main bars: #12 @ 100 mm c/c
Secondary bars: #12 @ 200 mm c/c
Cost of main re-bars: 105.25 INR
Cost of secondary re-bars: 52.63 INR

Total cost of re-bars: (132.92 x 11 + 66.46 x 11) + (105.25 x 11 + 52.63 x 11) INR = 3929.86 INR

Benefits:
(1) Average reduction in mid-span deflection (with respect to Q1-SS): 38% (Table-7)
(2) Average reduction in damage (with respect to Q1-SS): 61% (Table-10)
(3) Average reduction in crack depth of transverse cracks at mid-span on the tension side (with respect to Q1-SS): 32% (Table-13,15&16)